CHAPTER EIGHT

Flow dynamics of 3D multicellular systems into capillaries

Karine Guevorkian[1], **Françoise Brochard-Wyart**[1] **and David Gonzalez-Rodriguez**[2]

[1]Laboratoire Physico-Chimie Curie, Institut Curie, PSL Research University, Sorbonne Université, CNRS, Paris, France
[2]Université de Lorraine, LCP-A2MC, F-57000 Metz, France

8.1 Introduction

The life of a multicellular organism starts from a single cell, which grows, divides, differentiates, and forms various organs. Throughout this journey, cells experience mechanical cues such as internal or external forces, and geometrical constraints, affecting their motion and function. Hence, understanding how multicellular structures respond to mechanical signals is crucial to decipher mechanisms governing embryonic development or pathological events such as tumor formation and metastasis [1–3]. Mechanical signals induce cell shape changes, which in turn trigger biochemical responses, generating feedback loops [2,4]. During embryonic morphogenesis, forces at the tissue scale lead to cellular rearrangements, giving rise to collective responses, as observed in early stages of *Xenopus* [5,6] and *Drosophilla* [7,8] development, during embryonic elongation in *C. elegans* [9,10], as well as in chicken and zebrafish embryos [11–13].

The response of a material to an applied force is governed by its constitutive material properties. Multicellular living matter exhibits complex rheological behaviors [14,15], such as liquid-like [16] or solid-like [5,17,18] viscoelasticity, which determine their function [19]. In a seminal work, Steinberg and coworkers proposed an analogy between tissues and liquids to attribute a surface tension to soft embryonic tissues [16], which explained their mutual enveloping capacity [20]. In this picture, the surface tension is a direct consequence of cellular cohesion, which may be

Viscoelasticity and Collective Cell Migration.
DOI: https://doi.org/10.1016/B978-0-12-820310-1.00008-2

modified by individual cellular cortical tension [21]. Similarly, viscosity can be defined for liquid-like tissues as a measure of the resistance to cellular rearrangement in a stressed tissue [22,23]. In vivo tissues actively adjust their rheological properties, in space and time, to properly execute morphogenetic events [14,24–27], making the cross-talk between signaling and mechanics very rich to explore.

The experimental techniques to study tissue mechanics can be divided into three major groups. The first group consists of techniques that provide information about local material properties of the tissue and hence can be used to study rheological variations over the cell scale. Such techniques include atomic force microscopy [28] and active or passive microrheology [29–32]. The second group of techniques probe the intermediate scale between the cell and the tissue. They consist of cell-size deformable probes, inserted into a cellular aggregate of embryo to characterize local mechanical properties of the tissue [33–35]. Lastly, the third group of techniques measures global tissue mechanical properties by applying a controlled pull [36,37], by squeezing them between two plates at an imposed strain [16,23,38], or by aspirating them inside capillary tubes at a controlled stress [39,40].

In this chapter, we will focus on the technique of micropipette aspiration, which is a versatile tool [41–43] to study the mechanics of soft and biological systems over a large range of length scales spanning cell nucleus [44], single cell [45,46], developing mouse oocyte [47], cellular aggregates [40], tissues explants [39], and in vivo organs [48]. We will first detail key practical considerations to setup the technique, and then present a case study where micropipette aspiration serves to characterize the mechanical properties of spherical cellular aggregates. We will discuss the manifestations of cell activity in response to the applied stress, which modify the aggregate's rheological behavior. Then, we will describe how to characterize multicellular aggregate permeability by using a microfluidic system. We will close the chapter by discussing application perspectives of the aspiration technique.

8.2 Micropipette aspiration technique: a practical guide

We will open this chapter by giving a hands-on step-by-step guide for setting up a micropipette aspiration system, to study the mechanical

properties of multicellular systems such as cellular aggregates or tissue explants. The technique is rather simple and inexpensive, within the reach of biological laboratories. Moreover, as we will show later, the data analysis does not depend on the precise shape of the sample (cell aggregate, tissue explant, etc.), as long as the sample is large enough compared to the micropipette diameter, which facilitates the application of the technique to ex vivo tissue explants (Fig. 8.1D), organoids, and potentially to in vivo tissues.

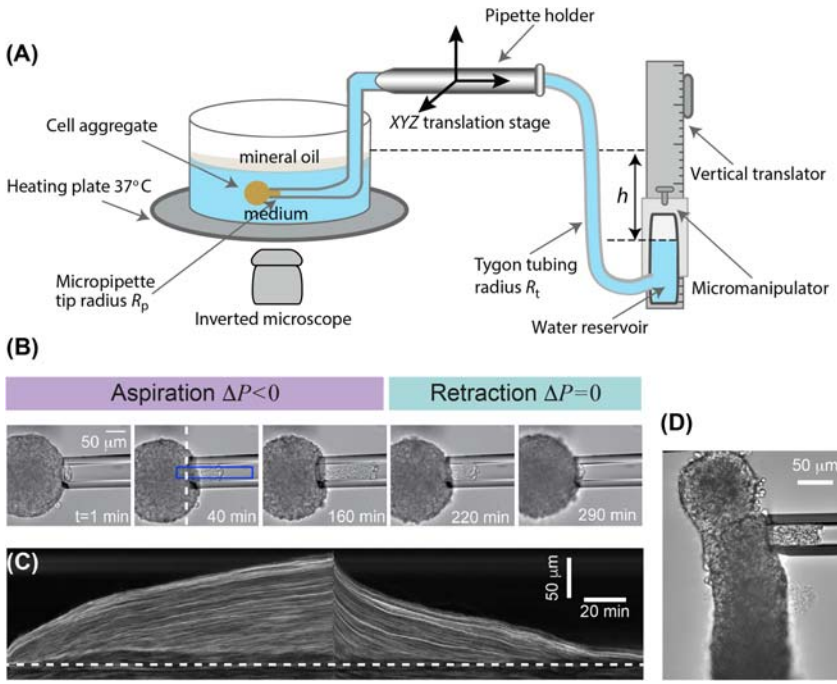

Figure 8.1 Micropipette aspiration technique. (A) The experimental setup. (B) Time series of the aspiration of an aggregate into a pipette at a pressure 1470 Pa (15 cm H_2O) for almost 3 hours, and retraction of the tongue as the aspiration pressure is set to zero. (C) Kymograph corresponding to the rectangular box in (B). The dashed line presents the entrance of the pipette, (D) Aspiration of the presomitic mesodermal tissue from a chicken embryo. *Images (B–C) are reproduced from K. Guevorkian, J.-L. Maître, Micropipette aspiration: a unique tool for exploring cell and tissue mechanics in vivo, in: Cell Polarity and Morphogenesis, Methods in Cell Biology, vol. 139, Academic Press, 2017, pp. 187–201 with permission.*

8.2.1 Preparation and mounting of glass micropipettes

The central element of this system is the micropipette. Therefore great care should be taken to obtain micropipettes with straight tips and long tapers to ensure the uniformity of the applied stress to the tissue. Conic tapers change the dynamics of aspiration and complicate the interpretation of the data. Preparation of the micropipettes takes place in two steps. First, the glass capillaries are extruded using a laser puller (Sutter Instrument, USA), and then the tip is scored at the desired diameter, either manually or by using a microforge instrument (Narishige, Japan). For multicellular samples, such as tissue explants or cell aggregates, the diameter of the micropipette tip should be at least 30–40 μm (several cell diameter) and can go up to few hundred micrometers if the sample is large enough. A microforge can be used to obtain diameters up to 50 μm, but for larger diameters, the tip should be scored manually, either using a ceramic tile (Sutter Instrument) or a second micropipette. Once the tip is scored, it should be fire-polished by gently approaching the tip to the heated wire of the microforge. Further information on the laser-puller parameters and scoring techniques can be found in The Pipette Cookbook [49]. We have found that borosilicate glass capillaries with 0.5 mm/1 mm (inner/outer) diameter yield the best tips for our experiments.

The shape of the micropipettes can be adapted to fit into the experimental chamber by simply heating the capillary with a flame or heated wire. For example, to introduce the pipette into a Petri dish, it should be bent in a step shape, as shown schematically in Fig. 8.1A. Simply hold the pipette with the desired bending location above a flame and let it bent under the action of its weight. This step should be performed before the passivation step.

Once the micropipettes are pulled and scored, they need to be passivated to prevent cells from adhering to the surface of the glass. To this end, we freshly prepare 0.1 mg/mL PolyEthyleneGlycol-PolyLysin (PLL(20)-g[3.5]-PEG(2), SuSos AG, Switzerland) solution in 7.3 pH HEPES from a 1 mg/mL stock solution. Note that this diluted solution can be kept at 4°C for up to 1 week. The coating is considerably enhanced if the pipette surface is activated in a plasma cleaner before the PEG-PLL treatment. For large tips such as the ones used here, spontaneous capillary suction suffices to fill them with PEG-PLL. A piece of Parafilm is placed in a large Petri dish, and 30–50 μL PEG-PLL drops are deposited on the

Parafilm. With the help of a spacer, which can be made of modeling paste, the pipettes are positioned slightly tilted, with one pipette tip in each drop. One can verify that liquid runs up the pipette tip within few seconds. To preserve the humidity, small pieces of wet paper tissues are placed in the Petri dish, which is then closed with the cover. For the passivation to take effect, this setup should be kept for 1 hour at room temperature. For an experiment the following day, micropipettes can be left in the drops overnight at 4°C, but care should be taken to prevent the drops from drying up. Before use, the pipettes are rinsed with PBS solution.

To connect the micropipettes to the pressure system, a micropipette holder (Narishige, Japan) is used, which in turn is mounted on an XYZ translation stage, as shown in Fig. 8.1A. The other end of the micropipette holder is connected to the water reservoir via Tygon tubing. The three-dimensional micromanipulator is used to navigate the pipette inside the experimental chamber. Once the sample to be aspirated has been located, a very small pressure is applied by lowering the pressure system just enough to hold the sample by sucking it slightly. Then we raise the pipette a few hundred micrometers above the bottom of the chamber to prevent contact between the sample and the bottom of the chamber during the experiment.

8.2.2 Experimental chamber

The choice of the experimental chamber depends on the volume of the medium available for experimentation. For small volume, a sheet of parafilm can be folded several times to give a U-shaped band of 5 mm × 5 mm × 5 cm. The band is then sandwiched in between the coverslip and the slide by gently heating the slide on a heating plate and compressing the system from the top. To assure the sealing, VALAP (Vaseline, Lanolin, Paraffin 1:1:1) can be used at the contours. The aggregates and the micropipette are then introduced from the open side, which is later sealed by injection of mineral oil (M5904, Sigma-Aldrich) at the interface to prevent evaporation.

If the volume of the solution is not a limiting factor, we suggest using Petri dishes as experimental chambers, because the aggregates (or tissue explants) survive longer in larger volumes of culture medium. In this geometry, the micropipette needs to be bent to enter the dish, as discussed above. Once the pipette is positioned, the top of the dish is covered with a thin layer of mineral oil.

8.2.3 Pressure system

In our experiments we use a water reservoir system to create a suction pressure, as shown in Fig. 8.1A. A 50 mL home-made plastic or plexiglass reservoir, connected with a Tygon tubing to the micropipette holder, is mounted on a micromanipulator, which in turn is mounted on a vertical linear translator. The micromanipulator allows precise positioning of the water reservoir, of particular importance for locating the null pressure. The vertical translator with a large step size (UniSlide Rapid advance, Velmex Inc., USA) is used to change the pressure quickly.

Before each experiment, it is essential to level the height of the water reservoir with the liquid in the chamber, such that there is no pressure difference. The position of the *zero* pressure is found by locating the exact position of the water reservoir where a trapped small debris in the micropipette does not get sucked in or pushed out. A pressure difference is applied by simply lowering the reservoir by a distance h, which yields a suction pressure: $\Delta P = \rho g h$, where ρ is the water (medium) density $\approx 1000\ \mathrm{kg/m^3}$, and $g = 9.81\ \mathrm{m/s^2}$ is the gravitational acceleration. We note that the volume of the thin layer of oil is negligible and does not change the density.

In this system the accuracy of the applied pressure is around 20 Pa, which is much smaller than the suction pressures used for soft tissues (ranging from 100 Pa to 5 kPa). An alternative to the water reservoir system is a microfluidic pump, as has been described elsewhere [42].

8.2.4 Aggregate preparation

In the experiments described in this chapter, murin sarcoma (S180) cell lines transfected to express E-Cadherin molecules [50] were used. This technique to produce spherical aggregates can be applied to other cell lines as well. The cells were cultured under 5% CO_2 atmosphere in DMEM enriched with 10% calf serum. Confluent cells were detached by incubation in Trypsin/EDTA for 5 minutes, diluted in CO_2 equilibrated culture medium, and centrifuged for 3 minutes at 1300 rpm. The pellets were resuspended in 5 mL of CO_2 equilibrated medium, at a concentration of 400,000 cells/mL, in 25 mL Erlenmeyer flasks that are placed in an orbital shaker at 75 rpm at 37°C for 18–24 hours, similar to procedures described in Ryan et al. [51]. With this technique, spherical aggregates of sizes varying from 100 to 500 μm in diameter were obtained. Before each experiment, aggregates were resuspended in

CO_2-independent medium enriched with glucose and 10% calf serum and transferred into the experimental chamber. Spherical cellular aggregates can also be prepared using the traditional hanging-drop technique [52] or microwell systems [53].

8.2.5 Video microscopy and image analysis

The video imaging is performed using an inverted microscope, functioning in bright field, equipped with $\times 10$ or $\times 20$ air objectives and a CCD camera. To observe cell rearrangements, confocal microscopy can be used as well. A heated microscope stage is used to keep the sample at 37°C. The image acquisition frequency varies between one frame per second to one frame per 30 seconds depending on the speed of aspiration and retraction. Fig. 8.1B shows a typical image sequence of an aspiration and retraction cycle, whereas Fig. 8.1D demonstrates the applicability of the technique to a mesoderm explant dissected from a 2-day chicken embryo.

To analyze the dynamics of the advancing tongue inside the pipette, manual tracking plugins available in Fiji (Image J) or custom-made automated routines can be used. A rapid and efficient way of observing and analyzing the dynamics is to use the kymograph modules available in Fiji (Image J) software as is shown in Fig. 8.1C for a typical aspiration/retraction cycle. A rectangular region is selected representing the whole aspirated tongue. Then, the Reslice function is used to produce a kymograph for each horizontal line in the form of a stack. To obtain the well-contrasted image presented in Fig. 8.1C, the Standard Deviation function in Fiji is applied to the stacks. Next, an edge-detection algorithm readily gives the aspiration and retraction profiles as a function of time. We have used this methodology to analyze the shivering profiles, as will later be discussed (Fig. 8.3A).

8.2.6 Microfluidic channels, alternatives to micropipettes

Besides their extensive use in single-cell studies, microfluidic channels can be used to study the flow properties of multicellular systems in confined geometries. Microfluidics have the advantage of providing channels of reproducible, precise dimensions as well as more complex geometries, like the one discussed in Section 8.6 to measure the permeability of cellular aggregates. However, in using these channels, few corrections should be brought to the analysis represented in the next section, to take into

account the noncircular cross-section of the channel, and the asymmetry imposed on the flow of the aggregate due to the flattening of the side of the sample facing the coverslip.

8.3 Viscoelastic behavior of cellular aggregates

Here we summarize how the micropipette aspiration technique reveals the viscoelastic characteristic of some embryonic tissues and tumors. An elastic material builds up stress upon deformation, and it regains its initial shape when the applied force is removed. The ratio of the applied stress (force per area), σ, to strain (deformation), ε, gives the elastic modulus, $E = \sigma/\varepsilon$. Thus a higher E denotes a material that is less deformable. In contrast, a viscous material deforms as long as the force is applied and does not regain its original shape once the force is removed. The dynamic viscosity coefficient is given by $\eta = \sigma/\dot{\varepsilon}$, where $\dot{\varepsilon}$ denotes the strain rate. Complex fluids, like living tissues, exhibit viscoelastic properties [23,55], meaning that unlike purely elastic or viscous materials, the nature of their response to an applied stress is time-dependent. The simplest type of viscoelastic behavior exhibits a characteristic time, $\tau \approx \eta/E$, which describes the transition from a short-time elastic regime into a long-time viscous regime.

The elastic and viscous properties of a tissue depend on several factors. The elasticity mainly depends on the structure of the extracellular matrix, the cell–cell adhesion, and the cellular cytoskeleton. The viscosity of a tissue originates from the dissipation due to cellular rearrangements. Moreover, when embryonic tissue explants are excised from the embryo, they round up to a final spherical form, like liquid drops, to minimize their surface energy. This is a manifestation of an effective surface tension [16,23], which has been related to the strength of cell–cell adhesion, for example, by modulating the expression of cadherin molecules, and to cortical tension [20,21].

To quantify viscoelastic parameters, spherical cellular aggregates are used as in vitro model systems for epithelial tissue. The advantages of these systems are that one can obtain aggregates of controlled and variable sizes, and modulate the strength of cell–cell adhesion by using cell lines expressing different levels of cadherin molecules.

8.3.1 Aspiration force and surface tension

Liquids tend to minimize the area of their free surface under the action of their surface tension. This is why an oil droplet in water will take a spherical shape. Cellular aggregates display a similar behavior, characterized by an effective surface tension arising from intercellular adhesion and cellular cortical tension [16,23]. The aspiration experiment shown in Fig. 8.1B–D demonstrates that once the aspiration pressure is released, the aspirated tongue is slowly reabsorbed inside the aggregate. Here, the restoring force is the effective surface tension, which is also the driving force in rounding experiments [56].

In the following we will derive the equations of a viscoelastic liquid model describing the aspiration of a cellular aggregate into a micropipette. We start by quantifying the net aspiration force deforming the aggregate, which, as we will see, is modified by the effect of its surface tension.

Let us consider an aggregate of resting radius R_0. We apply an aspiration pressure, ΔP, with a pipette of radius R_p, which corresponds to a total aspiration force $f_a = \pi R_p^2 \Delta P$. For large pressures, the aspirated length, L, inside the pipette will be larger than R_p, as shown schematically in Fig. 8.2A. In this case, the free energy of the system, F, is given by:

$$F = (4\pi R^2 + 2\pi R_p L)\gamma - \Delta P \pi R_p^2 L, \tag{8.1}$$

where γ is the effective surface tension of the aggregate, and R is the radius of the aggregate. Considering that volume is conserved during aspiration, we obtain:

$$\frac{4}{3}\pi R_0^3 = \frac{4}{3}\pi R^3 + \pi R_p^2 L \Rightarrow 4\pi R^2 \delta R + \pi R_p^2 \delta L = 0. \tag{8.2}$$

Therefore the effective aspiration force that contributes to aggregate deformation, $f = -\frac{\delta F}{\delta L}|_V$, is given by:

$$f = \pi R_p^2 (\Delta P - \Delta P_c), \tag{8.3}$$

where $\Delta P_c = 2\gamma\left(\frac{1}{R_p} - \frac{1}{R}\right)$ corresponds to Laplace's law and denotes a critical pressure above which the aggregate will flow inside the pipette. For $R \gg R_p$, the radius R of the aggregate can be considered constant, $R \approx R_0$, ΔP_c approximated by:

$$\Delta P_c = 2\gamma\left(\frac{1}{R_p} - \frac{1}{R_0}\right). \tag{8.4}$$

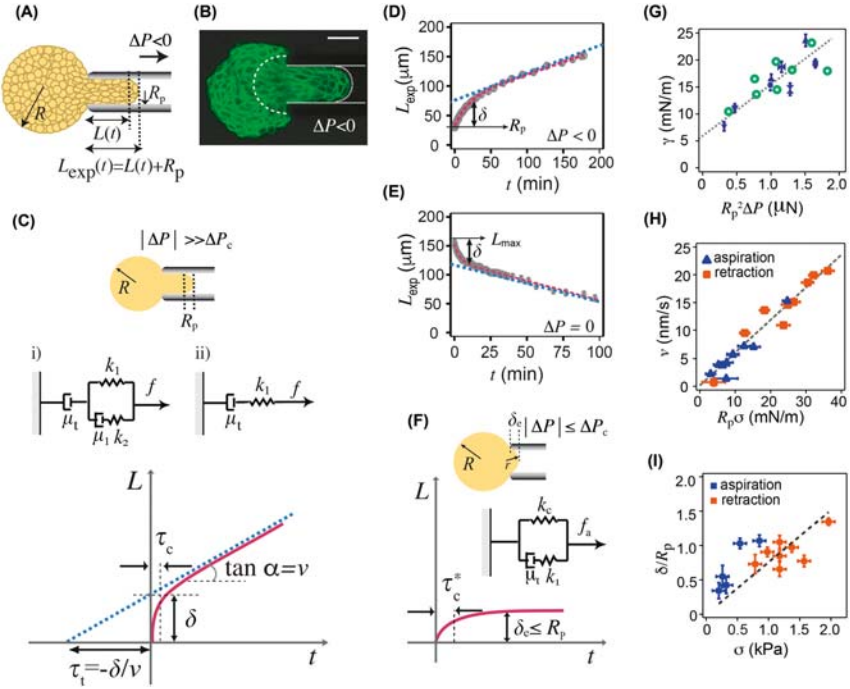

Figure 8.2 Rheology of cellular aggregates. (A) Schematic representation of an aspirated aggregate. (B) Confocal image of an aspirated aggregate, where the E-cadherins are tagged with GFP. The stretched cells can be observed inside the pipette and in the deformation zone within a radius R_p into the aggregate body depicted with the white dashed line. The pointed line shows the hemispherical cap, whose formation indicates the full development of the capillary resistance. $\Delta P = 500$ Pa, scale bar is 50 μm. (C) Schematic diagram showing the experimentally measurable parameters, and the rheological models for $\Delta P \gg \Delta P_c$. (i) the complete model with tissue and cell viscoelasticity (modified Kelvin−Voigt model), and (ii) a simplified model that neglects cell viscoelasticity (Maxwell liquid model). (D) Aspiration and (E) Retraction curves for an aggregate of radius $R_0 = 180$ μm and pipette radius $R_p = 35$ μm at $\Delta P = 1176$ Pa. Dashed lines are fits to the data using Eq. (8.12). (F) Schematic diagram showing the experimentally measurable parameters, and the rheological model for $\Delta P \leq \Delta P_c$. (G) Effective surface tension as a function of applied force. Open symbols are obtained from Eq. (8.17), filled symbols are from Eq. (8.16), and using the measured value of η. (H) Aggregate flow velocity as a function of stress. (I) Normalized deformation as a function of stress. *Image (B) is reproduced from K. Guevorkian, D. Gonzalez-Rodriguez, C. Carlier, S. Dufour, F. Brochard-Wyart, Mechanosensitive shivering of model tissues under controlled aspiration. Proc. Natl. Acad. Sci. U.S.A. 108 (33) (2011) 13387−13392 and images (D, E, G, H) are reproduced from K. Guevorkian, M.J. Colbert, M. Durth, S. Dufour, F. Brochard-Wyart. Aspiration of biological viscoelastic drops. Phys. Rev. Lett. 104 (2020) 218101 with permission.*

We note that for the case where $\Delta P \leq \Delta P_c$, the aggregate will respond with a small deformation $\delta_e \leq R_p$, as shown schematically in Fig. 8.2F, and the aggregate does not flow at long time. In this regime, $\Delta P = 2\gamma\left(\frac{1}{r} - \frac{1}{R_0}\right)$, where r is the radius of curvature of the aspirated protrusion. r is related to the deformation δ_e through

$$\frac{1}{r} = \frac{2\delta_e}{R_p^2 + \delta_e^2}. \tag{8.5}$$

Because in this regime $r > R_p$, the amount of pressure resisted by the surface tension is smaller than ΔP_c. This regime ends when the applied aspiration pressure becomes $\Delta P = \Delta P_c$, which corresponds to $\delta_e = r = R_p$. At this threshold of pressure, the capillary response of the aggregate is fully developed, as demonstrated by the formation of a hemispherical cap at the end of the tongue, as seen in Fig. 8.2B. Beyond this critical aspiration pressure (corresponding to a maximal capillary force $f_{c\,\max} = \pi R_p^2 \Delta P_c$), the aggregate flows over a long time. In this second regime of larger deformation, the effective aggregate rheology can be represented by Fig. 8.2C(i), with a net force for aggregate deformation f given by Eq. (8.3).

We can use Laplace's law to measure the surface tension of aggregates as follows. We start by applying a weak aspiration pressure, which we then increase in small steps while monitoring the length of the tongue L. When $L = R_p$, ΔP equals ΔP_c, from which γ can be estimated. While measuring precisely the pressure at which $L = R_p$ remains tedious due to the slow dynamics of the system, this method provides a rough estimate for γ, which in the case of aggregates of S180 murin sarcoma cell lines used in our studies is $5\ \text{mN/m} < \gamma < 7\ \text{mN/m}$. Note that the surface tension measured with this technique denotes the surface tension of the aggregate at rest, which we refer to as γ_0 in Section 8.3.5. We will later discuss a second approach to measure the surface tension, which can be obtained from the dynamics of aspiration.

8.3.2 Elastic deformation

Now let us look at the aspiration dynamics inside the pipette when the aggregate is subjected to a large constant strain $\sigma = f/A_0$, where $A_0 = \pi R_p^2$, leading to $\sigma = \Delta P - \Delta P_c$. Fig. 8.2B shows a typical creep curve with two distinct regimes; a rapid deformation defined by δ, followed by a constant flow at a rate v. Similar behavior has also been

observed for Chinese hamster ovary cell aggregates, using the parallel plate compression technique [57].

Taking the strain $\varepsilon = \delta/R_p - 1$, we obtain

$$E = \frac{\sigma}{\varepsilon} = C_e \frac{R_p(\Delta P - \Delta P_c)}{\delta - R_p}. \tag{8.6}$$

The constant C_e has been calculated numerically and shown to depend on geometric parameters such as the ratio between sample size and the pipette radius as well as to the wall thickness of the pipette tip [39]. For our experimental conditions $C_e \simeq 1$.

Similarly, over a long time, the aggregate behaves as a viscous fluid flowing at a constant velocity v, as we discuss below. The strain rate is $\dot{\varepsilon} = v/R_p$, leading to the viscosity:

$$\eta = \frac{\sigma}{\dot{\varepsilon}} = \frac{1}{C_v} \frac{R_p(\Delta P - \Delta P_c)}{v}, \tag{8.7}$$

where the coefficient C_v depends on the geometry. Also note that in order to measure the aggregate viscosity, intercellular friction must be the dominant dissipation mechanism, as we discuss in the next section.

8.3.3 Viscous dissipation

Based on experimental observations, aggregate flow into the pipette is assumed to exhibit a plug flow profile. Moreover, in the following discussion we will assume aggregate permeability to be negligible, meaning that the aggregate does not behave as a porous material. In Section 8.6 we will revisit this assumption, and confirm that porosity is negligible for the aggregates used in this study. We will discuss the modifications to the equations needed if tissue porosity becomes important.

The dissipative forces have several origins: (1) the viscous deformation of the aggregate as it penetrates into the pipette, f_v, (2) the friction of the aggregate sliding over the micropipette wall, f_w, and (3) the viscous dissipation due to the flow of liquid along the tube connecting the pipette and the water reservoir, f_l. Therefore the total dissipative force, f_{diss} is

$$f_{\text{diss}} = f_v + f_w + f_l. \tag{8.8}$$

$f_v = C_v \pi \eta R_p v$, where η is the viscosity of the cell aggregate, results from the rearrangement of the cells with respect to one another at the entrance of the micropipette. The numerical factor C_v has been calculated

analytically for the entrance of a viscous liquid inside an orifice and shown to be: $C_v = 3\pi$ [58]. The validity of this coefficient for a cylindrical capillary has been verified experimentally by studying the dynamics of extraction of a viscous oil through a nonadhesive capillary [59].

Now let us consider the dissipation caused by the sliding of the aspirated tongue on the micropipette with a friction coefficient k. The friction force is given by $f_w = 2\pi R_p k L v$, which depends on the length L of the aspirated tongue. For L much larger than the critical length $L_c = \frac{3\pi\eta}{2k}$, f_w dominates over f_v, leading to $L \sim t^2$, whereas when $L \ll L_c$, $L \sim t$. We have estimated k and L_c by aspirating an aggregate entirely inside a pipette at a constant suction pressure ΔP and measuring its advancement speed v. Once the aggregate is completely inside the pipette, $\Delta P_c = 0$ and $f_v = 0$, therefore from 3 we obtain

$$\pi R_p^2 \Delta P = 2\pi R_p k L^* v, \tag{8.9}$$

where L^* is the length of the aggregate slug inside the micropipette. For the case where the micropipette surface is rendered nonadhesive, for example, through PEG-PLL coating, we obtain $k \approx 10^8$ Pa s/m. Taking the value of $\eta \approx 10^5$ Pa s, $L_c \sim 5\ \mathrm{mm}^{-1}$ cm. Because the length of the tongue in our experiments does not exceed a few hundreds of micrometers, f_w is negligible compared to f_v. This is confirmed by the observation of a constant v ($L \sim t$) over the duration of our experiments, as mentioned above.

In the absence of aggregate permeability, the dissipation due to viscous liquid flow inside the tube induced by the aggregate motion is given by $f_l = 8\pi\eta_l l_t v \times \left(\frac{R_p}{R_t}\right)^4$, where l_t and R_t are the length and the radius of the tube, respectively. The critical tube length above which the effect of f_l becomes important is $l_t^* = \frac{3\pi}{8}\frac{\eta}{\eta_l}\left(\frac{R_t}{R_p}\right)^4 R_p$. In our experiments, $R_p/R_t \approx 0.1$, $20 < R_p < 50\ \mu$m, and $\eta_l = 10^{-3}$ Pa s. Taking $\eta \approx 10^5$ Pa s [60], $l_t^* \approx 10^7$ m, meaning that for cellular aggregates where $\eta \gg \eta_l$, f_l is negligible.

Therefore the relevant dissipation only occurs at the entrance of the micropipette, yielding the following relationship for the viscosity η:

$$\eta = \frac{R_p(\Delta P - \Delta P_c)}{3\pi v}. \tag{8.10}$$

8.3.4 Rheological models for aggregate flow into the capillary

As mentioned above, the cell aggregates behave like a viscoelastic solid at short times, and like a viscous liquid at long times, as can be seen from the creep curve shown in Fig. 8.2C. To combine these two regimes, we use a modified Kelvin–Voigt model as shown in Fig. 8.2C(i) consisting of a Kelvin–Voigt body built by two springs with constants k_1 and k_2 and a dashpot with constant μ_1, connected in series to a dashpot with constant μ_t. This four-element system accounts for three regimes: a very fast, purely elastic response seen as a jump at the beginning of the experiment, a viscoelastic solid-like behavior, and a long-term fluid flow. The displacement $L(t)$ of the tongue is given by

$$L(t) = \frac{f}{k_1}\left(1 - \frac{k_2}{k_1 + k_2}e^{-t/\tau_c}\right) + \frac{f}{\mu_t}t. \tag{8.11}$$

The first term represents the viscoelastic solid behavior. At $t \to 0$, there is a fast elastic jump given by $f/k_1 + k_2$, then after a characteristic time $\tau_c = \frac{\mu_1(k_1+k_2)}{k_1 k_2}$ the deformation reaches a value $\delta = f/k_1$. The second term describes the viscous flow characterized by a constant velocity $v = f/\mu_t$. We can express these mechanical parameters in term of E and η, using Eq. (8.3) with Eqs. (8.6) and (8.10), leading to $k_1 = \pi R_p E$ and $\mu_t = 3\pi^2 R_p \eta$. Similarly, $\mu_1 = \pi R_p \eta_c$ and τ_c describe the cell-scale viscoelasticity. Another relevant timescale is the one describing the transition of the tissue from the elastic regime to the viscous regime, which is given by $\tau = \mu_t/k_1 = 3\pi\eta/E$.

As discussed in Section 8.3.1, Eq. (8.11) is only valid for $\Delta P > \Delta P_c$ in which the length L refers to the aspirated tongue, excluding the hemispheriacal cap (see Fig. 8.2A). However, the experimentally measured length, L_{exp}, includes the hemospherical cap of radius R_p as shown schematically in Fig. 8.2A. Therefore, in order to employ Eq. (8.11) to adjust the data, we should apply the correction $L = L_{\text{exp}} - R_\text{p}$, as shown for the data in Fig. 8.2D. The aspiration dynamics for $\Delta P \leq \Delta P_c$ will be discussed below. It will be shown that in this regime, we reach a maximum deformation $\delta = R_p$ for $\Delta P = \Delta P_c$. On the other hand, we see that when $\Delta P = \Delta P_c$ from Eq. (8.11) we get $L_{\text{exp}} = R_\text{p}$, satisfying the continuity condition between the two regimes.

For simplicity, Eq. (8.11) can be written as the following:

$$L(t) = \delta\left(1 - \kappa e^{-t/\tau_c}\right) + vt, \tag{8.12}$$

where $\kappa = \frac{k_2}{k_1 + k_2}$. The viscoelastic parameters are obtained at each aspiration pressure by adjusting Eq. (8.12) to the aspiration and retraction curves with the following corrections:

$$\begin{aligned} L_{asp} &= L_{\exp} - R_p, \\ L_{ret} &= L_{\max} - L_{\exp}, \end{aligned} \tag{8.13}$$

where $L_{\max}$ is the maximum length of the aspirated tongue, just before the pressure is set back to zero, as shown in Fig. 8.2E.

If the cellular relaxation parameters, τ_c and μ_1, are not sought, the first rheological model in Fig. 8.2C(i) can be simplified to a Maxwell liquid model Fig. 8.2C(ii), consisting of a dashpot with constant μ_t in series with a spring, with spring constant k_1. This amounts to fitting a line to the linear viscous regime as shown with the dashed blue line in Fig. 8.2C–E. From the slope ν, and intercept δ, the viscosity and the elasticity can be deduced, as explained in Section 8.3.5.

Small ΔP regime

Let us now investigate the response of the aggregate when the aspiration pressure is smaller than the critical pressure ΔP_c. In this case, the resisting capillary force is smaller than that in the large pressure regime, $f_c < \pi R_p^2 \Delta P_c$. By applying Laplace's law to an aggregate aspirated by a length $L = \delta < R_p$, we obtain

$$f_c = \pi R_p^2 \times 2\gamma \left(\frac{2\delta}{\delta^2 + R_p^2} - \frac{1}{R_0} \right). \tag{8.14}$$

Assuming $R_0 \gg R_p$, Eq. (8.14) can be linearized in two limiting cases: (1) $\delta \ll R_p$, leading to $f_c \approx 4\pi\gamma\delta$, and (2) $\delta \approx R_p$, leading to $f_c \approx 2\pi\gamma R_p$. In both limits, the capillary force f_c is proportional to the deformation δ, suggesting that it can be represented by a (nonlinear) spring. To investigate the aspiration dynamics in this regime, we thus adopt the simple rheological model shown in Fig. 8.2F. Here, we add a spring of constant k_c, accounting for the restoring nature of the capillary effect, to our simplified Maxwell model for the tissue. Note also that, because in this regime the capillary resistance is included in the rheological model via the additional spring k_c, the force acting on the system is the total aspiration force, $f_a = \pi R_p^2 \Delta P$. The solution for this model is

$$\delta(t) = \frac{f_a}{k_c} \left(1 - \frac{k_1}{k_c + k_1} e^{-t/\tau_c^*} \right), \tag{8.15}$$

where $\tau_c^* = \frac{\mu_t(k_1 + k_c)}{k_1 k_c}$ is the characteristic time for the relaxation of elastic response. This analysis shows that for small aspiration pressures, the system will reach a finite deformation $\delta_e = f_a/k_c \sim \Delta P/\gamma$, up to a maximum value $\delta_e = R_p$ for $\Delta P = \Delta P_c$, beyond which the aggregate will flow at long time.

8.3.5 Rheological parameters for murin sarcoma cell aggregates

Here we will show the application of the above procedure to characterize the mechanical properties of S180 murin sarcoma cellular aggregates. The aspiration pressures used for these aggregates were between 1 and 3 kPa. In Fig. 8.2D–E we show an example of an aspiration and retraction cycle for $\Delta P = 1176$ Pa. The red dashed lines correspond to the adjustment of Eq. (8.12), with the corrections given by Eq. (8.13) accounted for. The blue dashed lines correspond to the simplified Maxwell model. We use the values of v^a and v^r, the flow rates during aspiration and retraction, respectively, to estimate the surface tension as follows. From Eq. (8.10), we have

$$\begin{aligned} v^a &= \frac{R_p(\Delta P - \Delta P_c)}{3\pi\eta} \\ v^r &= \frac{R_p \Delta P_c}{3\pi\eta} \end{aligned} \quad . \tag{8.16}$$

From this set of equations we can obtain ΔP_c as

$$\Delta P_c = \Delta P \times \frac{v^r}{v^a + v^r}. \tag{8.17}$$

For the specific set of experiments presented in Fig. 8.2D–E, we obtained $\Delta P_c = 690$ Pa. This pressure is significantly larger than the critical pressure that we would obtain from Laplace's equation, Eq. (8.4), with $\gamma_0 = 6$ mN/m ($\Delta P_{c0} = 300$ Pa). This suggests that γ has increased as a function of the applied pressure, ΔP. Indeed, Fig. 8.2G shows that the measured γ systematically increases as the applied force increases. We can estimate the surface tension of an aggregate at rest by extrapolation of the linear regression to the data, which gives $\gamma_0 = 6$ mN/m. This result is in agreement with the surface tension estimate that we obtain from measuring the critical Laplace pressure, as well as with the values reported for compression plate experiments [38]. We assume that the change in the

surface tension could be due to active responses of cells to the applied force. We will see in the next section that in certain aspiration conditions, this activity becomes directly observable. For comparison, in the case of an inert liquid, like an oil droplet, γ would not depend on the aspiration pressure.

Next, we investigate the dependence of the flow rate on the applied stress, σ. Note that during aspiration, $\sigma = (\Delta P - \Delta P_c)$, and during retraction $\sigma = \Delta P_c$. As can be seen in Fig. 8.2H, v has a linear relationship with $R\sigma$, in agreement with Eq. (8.10), where the slope yields $1/(3\pi\eta)$. The average value of the viscosity is $\eta = (1.9 \pm 0.3) \times 10^5$ Pa s.

An alternative way of deriving the viscosity, η, is by eliminating ΔP_c in Eq. (8.16), which gives the following relationship between viscosity and the flow rates:

$$\eta = \frac{R_p \Delta P}{3\pi(v^a + v^r)}. \tag{8.18}$$

For example, for the experiments in Fig. 8.2D–E, $\eta = 2.4 \times 10^5$ Pa s. We emphasize that in both of the proposed approaches to estimate η, ΔP_c is assumed not to change between the linear regimes of the aspiration and retraction curves.

The elastic modulus, E, can be obtained from the deformation δ, defined as the intercept of the linear flow regime and the vertical axis (see Fig. 8.2C–E). δ is related to the applied elastic stress by $\sigma_e = E\delta/R_p$. The stress during aspiration is $\sigma = \sigma_e = \Delta P - \Delta P_c$, whereas during the retraction, the net elastic stress is $\sigma_e = \Delta P$. Indeed, upon release of the applied aspiration pressure, the spring of constant k_1 is prestressed. Therefore the net change in elastic stress when the aspiration pressure is removed is $\sigma_e = \Delta P_c - (\Delta P - \Delta P_c) = \Delta P$. Therefore we have

$$\begin{aligned} \delta^a &= \frac{R_p(\Delta P - \Delta P_c)}{E}, \\ \delta^r &= \frac{R_p \Delta P}{E}, \end{aligned} \tag{8.19}$$

where δ^a and δ^r are the magnitudes of the deformation for aspiration and retraction curves, respectively. Fig. 8.2I shows the normalized δ, as a function of stress, where the inverse of the slope gives the average value $E = 1300 \pm 150$ Pa.

As shown in Fig. 8.2B, $\tau_t = \delta/v$ is obtained by the x-axis intercept of the linear fit to the experimental curve. Our estimated values

are $\tau_t^a = 2900 \pm 1100$ and $\tau_t^r = 1700 \pm 450$ seconds, obtained from the aspiration and the retraction curves, respectively. Using Eqs. (8.16) and (8.19), we find $\tau = 3\pi\eta/E = \tau_t^a = 2900 \pm 1100$ and $\tau = \tau_t^r \times (\Delta P_c/\Delta P) = 1200 \pm 200$ seconds. We thus notice a discrepancy between the τ obtained from the aspiration and retraction curves. However, on average we can estimate that the tissue relaxation time is of the order of few tens of minutes.

In summary, in this section we showed that cellular aggregates flow inside a cylindrical capillary like a viscoelastic liquid droplet when the applied pressure is in the range of 1−3 kPa. We then developed a mechanical model with two characteristic time scales; one at the cellular level, $\tau_c = \mu_1/k_1 \approx \eta_c/E \sim 100 - 200$ seconds, and one at the tissue level, $\tau = 3\pi\eta/E = 25 \pm 10$ minutes. The active response of the cells to the applied stress manifests itself in an increase of the effective surface tension. In the next section, we will further explore active cellular responses to an external stress.

8.4 Active response of cellular aggregates to mechanical stimuli

As discussed in the previous section, the active response of an aggregate to an external stress globally manifests itself with an increase of the effective surface tension. In this section, we explore the behavior of aggregates of smaller sizes in response to aspiration pressures that are weaker than previously explored. As will be demonstrated, in these specific conditions, we observe concrete signs of cellular mechanosensitivity, leading to pulsation of the aggregates. We present an analytical model that shows how these pulsations can be attributed to the active response of cells to stretching.

8.4.1 Aggregate pulsation or shivering

For pressures ranging between 500 Pa $\leq \Delta P <$ 1500 Pa, applied to aggregates measuring between 70− and 150 μm in radius, we observe unexpected pulsatile behavior of the aggregates that we call *shivering* [54]. This pulsatile behavior is suppressed when the aggregates are treated with 10 μM blebbistatin, which inhibits myosin II activity responsible for cell contraction, reinforcing the assumption that shivering originates from

cellular activity. The kymograph in Fig. 8.3A shows that, as the aggregate is aspirated inside the pipette, random contractions are detected inside the aspirated tongue. A careful observation of the kymograph reveals that, in

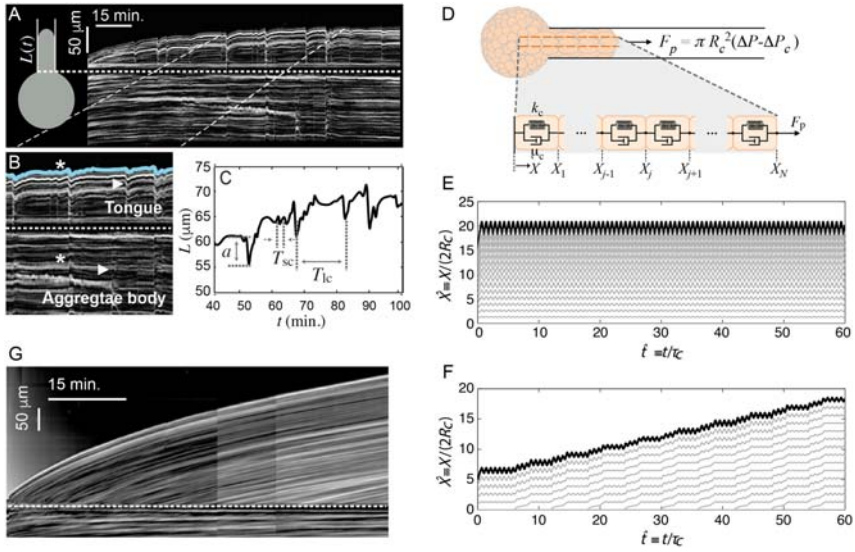

Figure 8.3 Shivering of a cellular aggregate under aspiration. (A, B) Kymograph showing the advancement $L(t)$ of the aggregate inside the pipette as a function of time, for an aggregate of $R_0 = 70$ μm and $R_p = 37$ μm, at a pressure of $\Delta P = 500$ Pa. (C) Tracking of the leading edge of (B), where a is the amplitude of the large contractions, and T_{sc} and T_{lc} are the periods of the small and large contractions, respectively. (D) One-dimensional model of aggregate shivering. Each cell is represented as a Kelvin–Voigt element to model the viscoelastic response of the cell. The viscous flow of the tissue is modeled by periodically adding one cell to the left end of the chain. (E) Aspiration curves predicted by the one-dimensional model for parameter values corresponding to a typical experiment ($\hat{F}_p = 0.5$, $N = 15$). The active cell response is characterized by $\hat{F}_m = 0.5$, $\epsilon_{crit} = 0.5$, $h = 100$, and $\hat{\tau}_s = 0.25$. The black curve corresponds to the position of the rightmost cell edge, X_N, and the gray curves correspond to the other cell edges along the chain. (F) Aspiration curves for the same parameter values but periodically increasing the number of cells to account for the viscous aggregate flow. The computation is started with $N = 5$ and one cell is added at the left end every 6 unit times, corresponding to the experimental observation that $\tau_{flow} \approx 6\tau_c$. The final number of cells is $N = 15$, as in the previous plot. (G) For similar aspiration conditions as in (A), with $\Delta P = 785$ Pa, the inhibition of Myosin II activity by blebbistatin treatment suppresses the shivering behavior and makes the aggregate more fluid. *Images (A–F) are reproduced from K. Guevorkian, D. Gonzalez-Rodriguez, C. Carlier, S. Dufour, F. Brochard-Wyart, Mechanosensitive shivering of model tissues under controlled aspiration. Proc. Natl. Acad. Sci. U.S.A. 108 (33) (2011) 13387–13392 with permission.*

some cases (shown with asters in the figure), these contractions are *global*, meaning that they are concomitant with a contraction in the aggregate body outside of the pipette. Other contractions are *local*, detected either in the tongue or in the body (shown with triangles).

To characterize these contractions, we develop an edge detection routine applied to the kymograph to determine the position of the advancing tongue inside the pipette as a function of time, as shown in Fig. 8.3B and C. We categorize two groups of contractions: (1) large contraction when the amplitudes is larger than 3 μm, (2) small contraction with amplitude ≈ 1 μm. For large contractions, we find a monotonic decrease of the amplitude from $a \approx 5$ μm for $\Delta P = 500$ Pa, down to $a \approx 1-2$ μm as the aspiration pressure increases to $\Delta P = 1200$ Pa. For each aspirated aggregate, we observe a few large contractions with period 500 seconds $< T_{lc} <$ 1000 seconds, and many small contractions with a period of $T_{sc} \approx 200$ seconds. We note that these aggregates have a $\Delta P_c \approx 200 - 300$ Pa, corresponding to $\gamma_0 \approx 5$ mN/m. For low aspiration pressures too close to ΔP_c, contractions are difficult to observe, because the aggregate barely enters the pipette, and for high $\Delta P > 1200$ Pa the amplitude of contraction becomes very small. Indeed, we did not see shivering for the experiments described in the previous section, where the aspiration pressures were larger than this threshold. In the following, we present a model to interpret these observations.

8.4.2 Model of delayed cell contraction

Our proposed model to interpret aggregate pulsation combines the viscoelastic behavior of a group of cells with a time-delayed active response. The latter hypothesis was inspired by a theoretical model previously developed to explain collective cellular oscillations during the dorsal closure in *Drosophilla* embryo [8]. Conveniently, in our system, the cells are confined in the cylindrical geometry of the micropipette tip, and subject to a unidirectional force, along the axis of the micropipette, which allows us to simplify the analysis to one dimension. Therefore to build our active mechanical model, we will simply analyze the response of a row of cells to a force applied to an imaginary pipette of radius R_c, equivalent to a cell radius, leading to $F_p = \pi R_c^2(\Delta P - \Delta P_c)$, as shown schematically in Fig. 8.3D. Here, we represent each cell as a Kelvin–Voigt element, with a spring constant $k_c = \pi R_c E$, and a dashpot of constant $\mu_c = \pi R_c \eta_c$. The applied force F_p stretches the cells along the array. If cell deformation

surpasses a critical strain $\varepsilon_{\text{shiv}}$, the cell will switch on an active contraction force F_m. Activation of this contraction force is not instantaneous, but rather it will occur after a time delay τ_s from the time when $\varepsilon_{\text{shiv}}$ is surpassed. This strain-dependent response can be expressed as

$$F_s(t) = \begin{cases} 0 & \text{if } \varepsilon(t-\tau_s) \leq \varepsilon_{\text{shiv}} \\ F_m & \text{if } \varepsilon(t-\tau_s) > \varepsilon_{\text{shiv}}, \end{cases} \tag{8.20}$$

where $F_s(t)$ is the contractile force that a cell exerts at time t when it has been strained by ε at time $(t-\tau_s)$. The corresponding continuum description is

$$\tau_c \frac{\partial \varepsilon}{\partial t} + \varepsilon = \frac{F_p - F_s}{2k_c R_c}. \tag{8.21}$$

where $\tau_c = \eta_c/E$ is the viscoelastic relaxation time of a cell. Integration of Eq. (8.21) yields

$$\varepsilon(\hat{t}) = \hat{F}_p\left(1 - e^{-\hat{t}}\right) + \varepsilon_c e^{-\hat{t}} - e^{-\hat{t}} \int_0^{\hat{t}} \hat{F}_m H(\varepsilon(\hat{\tau} - \hat{\tau}_s)) e^{\hat{\tau}} \mathrm{d}\hat{\tau}, \tag{8.22}$$

where H is the Heaviside function and the hat symbol, $\hat{}$, indicates quantities that are nondimensionalized using τ_c as the unit time and $2k_cR_c$ as the unit force. To simplify the writing, the hat symbols are omitted in what follows.

In this model, the shivering oscillations arise because of the active contractility switching alternatively on and off and making the cell deformation oscillate around $\varepsilon_{\text{shiv}}$. Because the constitutive equation is linear, the oscillation period T_{sc} is divided into a half period over which the active force is on and the cell contracts, and a half period over which it is off and the cell expands. To obtain the equation for $\varepsilon(t)$, we evaluate the integral in Eq. (8.21) taking as an initial condition $\varepsilon(t=0) = \varepsilon_{\text{shiv}}$. For $0 < t < \tau_s$, that is, before the active contraction force is switched on, Eq. (8.22) reduces to

$$\varepsilon(t) = F_p(1 - e^{-t}) + \varepsilon_c e^{-t}. \tag{8.23}$$

For $t > \tau_s$, the contractile force is switched on. As a result, if contraction is sufficiently strong, cell deformation decreases, and eventually becomes again smaller than $\varepsilon_{\text{shiv}}$. This occurs at $t = T_{sc}/2$. Therefore at the time $T_{sc}/2 + \tau_s$, the contraction force eventually switches back off. Integration of Eq. (8.22) for $\tau_s < t < T/2 + \tau_s$ yields

$$\varepsilon(t) = F_p(1 - e^{-t}) + \varepsilon_c e^{-t} - F_m(1 - e^{-(t-\tau_s)}). \tag{8.24}$$

Finally, we consider the time $T_{sc}/2 + \tau_s < t < T_{sc}$, when the active contraction is switched off. Integration of Eq. (8.22) yields

$$\varepsilon(t) = F_p(1 - e^{-t}) + \varepsilon_c e^{-t} + \frac{F_m(1 - e^{\tau_s})}{\varepsilon_c - F_p + F_m} e^{-(t-\tau_s)}. \tag{8.25}$$

The oscillation period T_{sc} is obtained by imposing that at the end of the period the cell recovers its initial deformation, that is, $\varepsilon(t = T_{sc}) = \varepsilon_c$. Returning hereafter to dimensional variables, we obtain the following relationship between the contraction period T_{sc} and the delay time τ_s:

$$e^{T_{sc}/\tau_c} = 1 + \frac{e^{\tau_s/\tau_c}\left(e^{\tau_s/\tau_c} - 1\right)}{\alpha(1 - \alpha)}, \tag{8.26}$$

where α has been defined by expressing the aspiration force as $F_p = F_{\text{shiv}} + \alpha F_m$, where $F_{\text{shiv}} = 2k_c R_c \varepsilon_{\text{shiv}}$ corresponds to the critical pressure required for shivering. We note that oscillations only arise if $F_{\text{shiv}} < F_p < F_{\text{shiv}} + F_m$, which corresponds to $0 < \alpha < 1$. Experimentally, we find that shivering happened when 500 Pa $< \Delta P <$ 1200 Pa. Taking $\Delta P_c \approx 300$ Pa gives us the range of $\frac{F_p}{\pi R_c^2} \approx 200 - 900$ Pa. This range is compatible with our model if we set $\frac{F_{\text{shiv}}}{\pi R_c^2} = (200 + 900)/2$ Pa and $\frac{F_m}{\pi R_c^2} = (900 - 200)/2$ Pa, which yields $\varepsilon_{\text{shiv}} \approx 0.3$ and $F_m \approx 0.1$ μN. The amplitude of the oscillations is the difference between the maximum and the minimum of $\varepsilon(t)$ given by Eqs. (8.24) and (8.25):

$$\Delta\varepsilon = \frac{F_m}{2k_c R_c}\left(1 - e^{-\tau_s/\tau_c}\right). \tag{8.27}$$

Experimentally, $2R_c\Delta\varepsilon \approx 2$ μm. According to Eq. (8.27) and taking $R_c \approx 15$ μm and $\tau_c \approx 200$ seconds this corresponds to a delay time $\tau_s \approx 40$ seconds. Finally, Eq. (8.26) with $\alpha \approx 1/2$ yields $T_{sc} \approx 150$ seconds.

To afford a visual comparison between the predictions of this model and the experiments, we numerically simulate the behavior of a string of cells aspirated in a micropipette. Each cell in the string was modeled as a Kelvin–Voigt element. Additionally, each cell exhibits an active delayed contractility, as described by Eq. (8.20). The simplest numerical simulation considers a fixed number of cells inside the pipette (Fig. 8.3E). Shivering arises if the applied aspiration pressure is large enough to bring cell stretching beyond the contractility threshold, but not too large, so that with contractility forces on, cell stretching is reduced below the threshold, thus switching contractility off again. The period of such oscillations is

proportional to the delay time τ_s. With a fixed number of cells in the pipette, our model predicts regular oscillations, which we interpret to correspond to the frequent small contractions in the experiment, of period $T_{sc} = 4\tau_s \approx 200$ seconds.

The observed large contraction could be explained by considering synchronous contractions of several cells, which could be associated with cell reorganizations due to aggregate flow into the pipette. Thus we have considered a modified version of our numerical model where the number of cells inside the pipette increases over time due to aggregate flow, shown in Fig. 8.3F. Cell flow into the pipette induces heterogeneities in the oscillation pattern, yielding a simulated kymograph that more closely resembles the experimental one. In our experiments, we have noticed that shivering is more frequent in smaller size aggregates. This might be related to the ratio of the deformed volume of the aggregate body $\sim R_p^3$ to the total volume. A more systematic study should addressee this hypothesis. We also observe that interfering with myosin II activity, by 10 μM blebbistatin treatment, suppresses the contractions, and also makes the aggregate flow easier, as can be seen in the kymograph shown in Fig. 8.3G.

8.5 Permeability of cellular aggregates

Interstitial flow plays an important role in tissue morphogenesis, function, and pathology [61]. It is most prominently linked to the drainage of blood plasma leaking from capillaries toward lymphatic vessels. Interstitial flow occurs through the extracellular matrix. In tissues with little extracellular matrix or in model tissues lacking an extracellular matrix, interstitial flow is controlled by permeability at the intercellular junctions, which depends on the strength of intercellular adhesions.

Cellular aggregate permeability can be characterized by microfluidics. By placing a cellular aggregate in a specially designed chamber in a microfluidic channel, as sketched in Fig. 8.4A, an interstitial flow can be imposed through it. The aggregate permeability can be quantified by assuming the aggregate to behave as a porous medium following Darcy's law, that is,

$$Q = \frac{\Delta P}{R_h}, \tag{8.28}$$

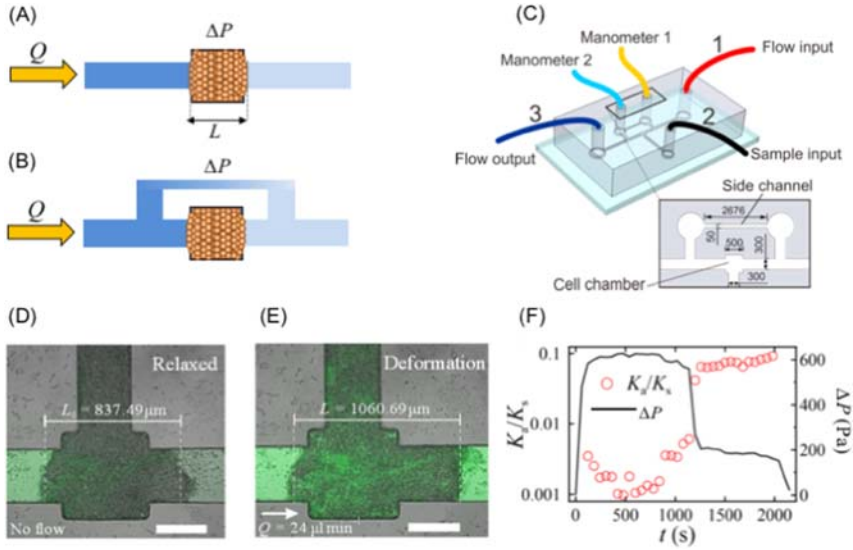

Figure 8.4 Permeability of cellular aggregates. (A) Principle of characterization of aggregate permeability in a microfluidic channel and (B) usage of a side channel to prevent experimental artifacts. The practical realization of this idea is shown in (C), with dimensions in micrometer. (D, E) Experimental images of the measurement of permeability of a MCF-7 cellular aggregate in a microfluidic channel. A fluorescent tracer has been used to visualize the advancement of the flow through the aggregate, which goes from left to right. The scale bar corresponds to 200 μm. (F) Experimental measurement of the intrinsic permeability of a MCF-7 cellular aggregate, K_a, in the microfluidic system shown in (C). The intrinsic permeability of the side channel is here $K_s = 1.97 \times 10^{-10}$ m^2. In this experiment, aggregate fracture occurs at $t \approx 1200$ seconds, as indicated by the sudden drop of the pressure difference, causing K_a to increase. *Images (C–F) are reproduced from Q.D. Tran, M. Marcos, D. Gonzalez-Rodriguez. Permeability and viscoelastic fracture of a model tumor under interstitial flow. Soft Matter 14 (2018) 6386–6392 with permission from the Royal Society of Chemistry.*

where Q is the flow rate through the aggregate for an imposed pressure difference ΔP, and $R_h = \eta_l L/(K_a A)$ is the aggregate's total hydrodynamic resistance, which depends on the medium fluid viscosity η_l, the aggregate's length along the flow direction L and cross-section A, and the aggregate's intrinsic permeability K_a. By imposing Q and measuring ΔP or vice versa, the intrinsic permeability can be determined.

In practice, experimental difficulties may prevent the realization of the setup in Fig. 8.4A. Tran et al. [62] attempted to realize this setup by imposing a flow rate through the aggregate using a syringe pump, and by measuring the resulting pressure difference across the aggregate by means

of a manometer. Due to the low permeability of the MCF-7 breast cancer cell aggregates used in their study, which would require to impose a very small flow rate, the setup proved impractical. To overcome this difficulty, they proposed an alternative setup with a narrow side channel parallel to the aggregate chamber, as sketched in Fig. 8.4B and C. The side channel permeability is carefully chosen to allow sufficient continuous flow for proper operation of the system while at the same time not overshadowing the permeability of the sample. Using this setup, an aggregate permeability $K_a = (8 \pm 5) \times 10^{-13}\ \mathrm{m}^2$ was measured, as shown in Fig. 8.4F [62]. The large standard deviation reflects significant variability both between samples and over time, as well as a measurement uncertainty introduced by the permeability of the side channel. We also note that the permeability is associated with a characteristic length $\sqrt{K_a} \approx 1\ \mu\mathrm{m}$, comparable to the intercellular distance within the aggregate.

The picture of aggregate permeability as that of a porous medium governed by Darcy's law is a highly simplified one. In reality, aggregate deformation induced by flow will modify its permeability, as suggested by the experimental images in Fig. 8.4D and E. At moderate flow rates, permeability increases due to viscoelastic deformation, whereas larger flow rates induce the formation of cracks through the aggregate that highly permeabilize it. This latter phenomenon is known as "aggregate fracture" under flow. MCF-7 aggregates of a few hundred micrometers in size fracture under flow pressures of the order of 500 Pa [62,63]. We note that in this setup aggregate flow is prevented due to strong adhesion to the device walls, here treated with fibronectin. This differs from the micropipette experimental system, where the pipette walls are rendered nonadhesive. This is why pressure values of about 500 Pa do not induce fracture in the micropipette experiment. When discussing aggregate fracture, we must also keep in mind that the meaningful fracture threshold is prescribed by the intercellular adhesion energy, G. Indeed, it can be shown that the aforementioned pressure threshold is linked to an intercellular adhesion energy of the order of $G \approx 10^{-2}\ \mathrm{J\,m}^{-2}$, a value that has been reported for aggregates of different cell lines [36,62]. A simple relationship between pressure threshold ΔP_{frac} and adhesion energy G can be written for fast loading, under which the aggregate behaves elastically. In this case, $G \sim \Delta P_{\mathrm{frac}}(L_{\mathrm{frac}} - L_0) = \Delta P_{\mathrm{frac}}^2 L_0 / E$. With $L_0 \approx 100\ \mu\mathrm{m}$ and $E \approx 1\ \mathrm{kPa}$, this simplified equation explains the relationship between the orders of magnitude of ΔP_{frac} and G. Future work is still required to fully characterize aggregate permeability. Open questions are the dependence of aggregate

permeability on deformation, the respective roles of intercellular adhesion energy and of the extracellular matrix, and a theoretical modeling of aggregate permeability experiments that includes poroelastic effects [64].

When studying a permeable sample, the equations describing micropipette aspiration discussed in Section 8.3.3 may need modification. Indeed, for a permeable aggregate, the flow velocity of the medium inside the pipette will no longer be equal to the velocity v of advancement of the aggregate tongue, as was stated in Section 8.3.3 for an impermeable aggregate. Rather, the medium flow velocity will scale as $v_l \sim K_a \Delta P/(\eta_l L)$, where L is the length of the aspirated tongue. The ratio between the viscous dissipation due to aggregate deformation, f_v, and viscous dissipation due to flow of medium, f_l, yields a new critical length, $L_c^{'} = 8K_a R_p^2 l_t / R_t^4$. Permeability effects can be neglected if $L \ll L_c^{'}$. For a typical cellular aggregate permeability $K_a < 10^{-12}$ m^2 in the experimental conditions described in Section 8.3.3, we obtain $L_c^{'} > 1$ m, which justifies neglecting permeability effects when studying cell aggregate viscoelasticity. We emphasize that $L \ll L_c^{'}$ means that the total aspiration pressure exerted on the aggregate is not affected by permeability, but it does not preclude the existence of interstitial flow, $v_l > v$. The condition for interstitial flow velocity to be significant compared to aggregate deformation speed is $L > L_{\text{perm}} = (K_a \eta)/(R_p \eta_t)$. When $L \gtrapprox L_{\text{perm}}$, part of the aspiration force is exerted on the aggregate as a shear stress of the interstitial fluid, which may yield to different physics of tissue deformation. In our experimental conditions, $L_{\text{perm}} \approx 1$ m and this effect is again negligible.

If the aggregate is sufficiently permeable, interstitial flow could be measured in the micropipette experiment by tracking the motion of debris downstream of the aspirated tongue. This would provide an estimate of the interstitial flow speed v_l, which is expected to depend on the aspirated length L. By measuring $\Delta v = v_l - v$ as a function of L, intrinsic permeability K_a can be deduced by fitting the equation

$$\frac{1}{\Delta v} = \frac{\eta_l}{K_a \Delta P}(L_a + L), \tag{8.29}$$

where L_a is an unknown constant accounting for the hydraulic resistance contributed by the aggregate body outside the pipette. Eq. (8.29) assumes the aggregate's permeability K_a to be a constant, independent of the aggregate's deformation. An alternative hypothesis, which can be tested experimentally, is that K_a increases with increasing ΔP due to increasing elastic deformation, that is, a poroelastic effect.

8.6 Conclusions and perspectives

In this chapter, we studied the flow of cellular aggregates into capillaries. Under constant stress conditions, the flow dynamics reveal the viscoelastic liquid behavior of these model tissues. At short time, we observe a fast deformation regime related to an elastic response. At long time, the tissue flows at a constant speed, thus behaving like a viscous liquid. We developed a methodology to extract elastic and viscous coefficients, as well as an effective surface tension, from the information contained in the aspiration and relaxation curves at constant pressure. In this description we consider the aggregates to be impermeable, a condition that is satisfied in our experiments but that may not always be valid. To address this question, we present a microfluidic system that allows measuring the permeability of cell aggregates and tissue explants. Microfluidic experiments confirm that permeability effects are negligible in our micropipette experiment conditions. However, porosity can be important in other tissue types and play a crucial role in their function, as has been observed recently in the case of cancer tumors [31]. We have thus discussed how to analyze micropipette aspiration experiments of tissues with significant permeability.

To address the increasing interest in understanding the role of rheology in morphogenesis and disease [19], the approaches developed in this chapter can readily be applied to embryonic tissues. In a recent study, micropipette aspiration has been applied to explants of *Xenopus* embryos at the gastrulation stage, in order to investigate mechanical differences between ectoderm and mesoderm tissues and to correlate tissue mechanics to acto-myosin activity [65]. A similar approach has been used to put in evidence that bacterial aggregates of *Neisseria meningitidis* actively modulate their rheological properties to increase their colonization efficiency into narrow capillaries [66].

Besides rheological measurements, the pipette system allows exploration of tissue mechanosensitivity under controlled external stress. In the example discussed in this chapter, the active nature of a cellular aggregate reveals itself as pulsatile contractions both at cellular and multicellular scales. Strikingly, pulsation only arises over a limited range of moderate external stress, whereas at larger stress the tissue contracts permanently. Then, activity manifests itself less conspicuously, as a change of the apparent rheological properties of the tissue. Combined with confocal

microscopy, mechanisms of tissue intercalation can be studied when a controlled external stress is applied through micropipette aspiration, as has been used to study the role of growth factors such as FGF on vertex formation in mouse embryonic limb bud ectoderm [67].

The micropipette aspiration technique has been widely used in the past several decades for studies on single cells and biomimetic systems, such as giant unilamellar vesicles. However, its application to living tissues is at its dawn. The few examples discussed here show its potential for application to multicellular systems, ranging from in vitro cellular aggregates to organoids, embryonic tissue explants, and even in vivo tissues.

Acknowledgments

We thank our colleagues who have worked with us on the research questions discussed in this chapter, most particularly Stéphane Douezan, Sylvie Dufour, Marcos, and Quang D. Tran.

References

[1] N.M.E. Ayad, S. Kaushik, V.M. Weaver, Tissue mechanics, an important regulator of development and disease, Philos. Trans. R. Soc. B 374 (1779) (2019).
[2] S. Suresh, Biomechanics and biophysics of cancer cells, Acta Biomater. 3 (4) (2007) 413–438.
[3] H. Yu, J.K. Mouw, V.M. Weaver, Forcing form and function: biomechanical regulation of tumor evolution, Trends Cell Biol. (2010) 1–10.
[4] D. Mitrossilis, J. Fouchard, A. Guiroy, N. Desprat, N. Rodriguez, B. Fabry, et al., Single-cell response to stiffness exhibits muscle-like behavior, Proc. Natl. Acad. Sci. U. S. A. 106 (43) (2009) 18243–18248.
[5] L.A. Davidson, S.D. Joshi, H.Y. Kim, M. vonDassow, L. Zhang, J. Zhou, Emergent morphogenesis: elastic mechanics of a self-deforming tissue, J. Biomech. 43 (1) (2010) 63–70.
[6] M. von Dassow, J.A. Strother, L.A. Davidson, Surprisingly simple mechanical behavior of a complex embryonic tissue, PLoS One 5 (12) (2010) e15359.
[7] B. Guirao, Y. Bellaïche, Biomechanics of cell rearrangements in Drosophila, Curr. Opin. Cell Biol. 48 (2017) 113–124.
[8] J. Solon, A. Kaya-Copur, J. Colombelli, D. Brunner, Pulsed forces timed by a ratchet-like mechanism drive directed tissue movement during dorsal closure, Cell 137 (7) (2009) 1331–1342.
[9] M. Ben Amar, P. Qiuyang-Qu, T.T.K. Vuong-Brender, M. Labouesse, Assessing the contribution of active and passive stresses in *C. elegans* elongation, Phys. Rev. Lett. 121 (2018) 268102.
[10] A. Lardennois, G. sti, T. Ferraro, F. Llense, P. Mahou, J. Pontabry, et al., An actin-based viscoplastic lock ensures progressive body-axis elongation, Nature (2019) 1–21.
[11] B. Bénazéraf, PF, R.E. Baker, N. Denans, C.D. Little, O. Pourquié, A random cell motility gradient downstream of fgf controls elongation of an amniote embryo, Nature 466 (7303) (2010) 248–252.

[12] A.K. Lawton, A. Nandi, M.J. Stulberg, N. Dray, M.W. Sneddon, W. Pontius, et al., Regulated tissue fluidity steers zebrafish body elongation, Development 140 (3) (2013) 573–582.
[13] A. Mongera, A. Michaut, C. Guillot, F. Xiong, O. Pourquié, Mechanics of antero-posterior axis formation in vertebrates, Annu. Rev. Cell Dev. Biol. 35 (1) (2019) 259–283.
[14] D. Bi, X. Yang, M.C. Marchetti, M.L. Manning, Motility-driven glass and jamming transitions in biological tissues, Phys. Rev. X 6 (2) (2016) 021011–021013.
[15] I. Bonnet, P. Marcq, F. Bosveld, L. Fetler, Y. Bellaiche, F. Graner, Mechanical state, material properties and continuous description of an epithelial tissue, J. R. Soc. Interface 9 (75) (2012) 2614–2623.
[16] R.A. Foty, G. Forgacs, C.M. Pfleger, M.S. Steinberg, Liquid properties of embryonic tissues: measurement of interfacial tensions, Phys. Rev. Lett. 72 (14) (1994) 2298–2301.
[17] L. Oswald, S. Grosser, D.M. Smith, J.A. Käs, Jamming transitions in cancer, J. Phys. D: Appl. Phys. 50 (48) (2017) 483001.
[18] T. Savin, N.A. Kurpios, A.E. Shyer, P. Florescu, H. Liang, L. Mahadevan, et al., On the growth and form of the gut, Nature 476 (7358) (2011) 57–62.
[19] N.I. Petridou, C.P. Heisenberg, Tissue rheology in embryonic organization, EMBO J. 38 (20) (2019) 1–13.
[20] R.A. Foty, C.M. Pfleger, G. Forgacs, M.S. Steinberg, Surface tensions of embryonic tissues predict their mutual envelopment behavior, Development 122 (5) (1996) 1611–1620.
[21] M.L. Manning, R.A. Foty, M.S. Steinberg, E.M. Schoetz, Coaction of intercellular adhesion and cortical tension specifies tissue surface tension, Proc. Natl. Acad. Sci. U. S. A. 107 (28) (2010) 12517–12522.
[22] R. David, O. Luu, E.W. Damm, J.W.H. Wen, M. Nagel, R. Winklbauer, Tissue cohesion and the mechanics of cell rearrangement, Development 141 (19) (2014) 3672–3682.
[23] G. Forgacs, R.A. Foty, Y. Shafrir, M.S. Steinberg, Viscoelastic properties of living embryonic tissues: a quantitative study, Biophys. J. 74 (5) (1998) 2227–2234.
[24] E.H. Barriga, R. Mayor, Adjustable viscoelasticity allows for efficient collective cell migration, Semin. Cell Dev. Biol. 93 (2019) 55–68.
[25] N. Khalilgharibi, J. Fouchard, P. Recho, G. Charras, A. Kabla, The dynamic mechanical properties of cellularised aggregates, Curr. Opin. Cell Biol. 42 (2016) 113–120.
[26] A. Mongera, P. Rowghanian, H.J. Gustafson, E. Shelton, D.A. Kealhofer, E.K. Carn, et al., A fluid-to-solid jamming transition underlies vertebrate body axis elongation, Nature 561 (7723) (2018) 401–405.
[27] B. Wallmeyer, S. Trinschek, S. Yigit, U. Thiele, T. Betz, Collective cell migration in embryogenesis follows the laws of wetting, Biophys. J. 114 (2018) 213–222.
[28] S. Tripathy, E.J. Berger, Measuring viscoelasticity of soft samples using atomic force microscopy, J. Biomech. Eng. 131 (9) (2009).
[29] A. D'Angelo, K. Dierkes, C. Carolis, G. Salbreux, J. Solon, *In vivo* force application reveals a fast tissue softening and external friction increase during early embryogenesis, Curr. Biol. 29 (9) (2019) 1564–1571.e6.
[30] K. Doubrovinski, M. Swan, O. Polyakov, E.F. Wieschaus, Measurement of cortical elasticity in *Drosophila melanogaster* embryos using ferrofluids, Proc. Natl. Acad. Sci. U. S. A. 114 (5) (2017) 1051–1056.
[31] Y.L. Han, A.F. Pegoraro, H. Li, K. Li, Y. Yuan, G. Xu, et al., Cell swelling, softening and invasion in a three-dimensional breast cancer model, Nat. Phys. (2019) 1–10.

[32] A.D. Wessel, M. Gumalla, J. Grosshans, C.F. Schmidt, The mechanical properties of early drosophila embryos measured by high-speed video microrheology, Biophys. J. 108 (8) (2015).
[33] O. Campàs, T. Mammoto, R.A. Hasso, S. Sperling, D. O'Connell, A.G. Bischof, et al., Quantifying cell-generated mechanical forces within living embryonic tissues, Nat. Methods 11 (2) (2014) 183–189.
[34] W. Lee, N. Kalashnikov, S. Mok, R. Halaoui, E. Kuzmin, A.J. Putnam, et al., Dispersible hydrogel force sensors reveal patterns of solid mechanical stress in multicellular spheroid cultures, Nat. Commun. 10 (1) (2019) 144.
[35] E. Mohagheghian, J. Luo, J. Chen, G. Chaudhary, J. Chen, J. Sun, et al., Quantifying compressive forces between living cell layers and within tissues using elastic round microgels, Nat. Commun. (2018) 1–14.
[36] D. Gonzalez-Rodriguez, L. Bonnemay, J. Elgeti, S. Dufour, D. Cuvelier, F. Brochard-Wyart, Detachment and fracture of cellular aggregates, Soft Matter 9 (7) (2013) 2282–2290.
[37] A.R. Harris, J. Bellis, N. Khalilgharibi, T. Wyatt, B. Baum, A.J. Kabla, et al., Generating suspended cell monolayers for mechanobiological studies, Nat. Protoc. 8 (12) (2013) 2516–2530.
[38] A. Mgharbel, H. Delanoë-Ayari, J.-P. Rieu, Measuring accurately liquid and tissue surface tension with a compression plate tensiometer, HFSP J. 3 (2009) 213–221.
[39] T. Aoki, T. Ohashi, T. Matsumoto, M. Sato, The pipette aspiration applied to the local stiffness measurement of soft tissues, Ann. Biomed. Eng. 25 (1997) 581–587.
[40] K. Guevorkian, M.J. Colbert, M. Durth, S. Dufour, F. Brochard-Wyart, Aspiration of biological viscoelastic drops, Phys. Rev. Lett. 104 (2010) 218101.
[41] B. González-Bermúdez, G.V. Guinea, G.R. Plaza, Advances in micropipette aspiration: applications in cell biomechanics, models, and extended studies, Biophys. J. 116 (4) (2019) 587–594.
[42] K. Guevorkian, J.-L. Maître, Micropipette aspiration: a unique tool for exploring cell and tissue mechanics in vivoMethods in Cell Biology, vol. 139 Cell Polarity and Morphogenesis, Academic Press, 2017, pp. 187–201.
[43] R.M. Hochmuth, Micropipette aspiration of living cells, J. Biomech. 33 (1) (2000) 15–22.
[44] F. Guilak, J.R. Tedrow, R. Burgkart, Viscoelastic properties of the cell nucleus, Biochem. Biophys. Res. Commun. 269 (3) (2000) 781–786.
[45] E. Evans, A. Yeung, Apparent viscosity and cortical tension of blood granulocytes determined by micropipet aspiration, Biophys. J. 56 (1) (1989) 151–160.
[46] J.L. Maître, H. Turlier, R. Illukkumbura, B. Eismann, R. Niwayama, F. Nédélec, et al., Asymmetric division of contractile domains couples cell positioning and fate specification, Nature (2016) 1–14.
[47] A. Chaigne, C. Campillo, N.S. Gov, R. Voituriez, J. Azoury, C. Umaña-Diaz, et al., A soft cortex is essential for asymmetric spindle positioning in mouse oocytes, Nat. Cell Biol. 15 (8) (2013) 958–966.
[48] A. Nava, E. Mazza, M. Furrer, P. Villiger, W.H. Reinhart, In vivo mechanical characterization of human liver, Med. Image Anal. 12 (2) (2008) 203–216.
[49] Sutter Instruments. Pipette cookbook. https://www.sutter.com/PDFs/pipette_cookbook.pdf.
[50] Y.S. Chu, W.A. Thomas, O. Eder, F. Pincet, E. Perez, J.P. Thiery, et al., Force measurements in e-cadherin mediated cell doublets reveal rapid adhesion strengthened by actin cytoskeleton remodeling through rac and cdc42, J. Cell Biol. 167 (6) (2004) 1183.

[51] P.L. Ryan, R.A. Foty, J. Kohn, M.S. Steinberg, Tissue spreading on implantable substrates is a competitive outcome of cell-cell vs. cell-substratum adhesivity, Proc. Natl. Acad. Sci. U. S. A. 98 (8) (2001) 4323–4327.
[52] R. Foty, A simple hanging drop cell culture protocol for generation of 3D spheroids, J. Vis. Exp. 51 (2011) e2720.
[53] Y.C. Chen, X. Lou, Z. Zhang, P. Ingram, E. Yoon, High-throughput cancer cell sphere formation for characterizing the efficacy of photo dynamic therapy in 3D cell cultures, Sci. Rep. 5 (1) (2015) 12175.
[54] K. Guevorkian, D. Gonzalez-Rodriguez, C. Carlier, S. Dufour, F. Brochard-Wyart, Mechanosensitive shivering of model tissues under controlled aspiration, Proc. Natl. Acad. Sci. U. S. A. 108 (33) (2011) 13387–13392.
[55] D. Gonzalez-Rodriguez, K. Guevorkian, S. Douezan, F. Brochard-Wyart, Soft matter models of developing tissues and tumors, Science 338 (6109) (2012) 910–917.
[56] J.C.M. Mombach, D. Robert, F. Graner, G. Gillet, G.L. Thomas, M. Idiart, et al., Rounding of aggregates of biological cells: experiments and simulations, Phys. A: Stat. Mech. Appl. 352 (2) (2005) 525–534.
[57] K. Jakab, B. Damon, F. Marga, O. Doaga, V. Mironov, I. Kosztin, et al., Relating cell and tissue mechanics: implications and applications, Dev. Dyn. 237 (9) (2008) 2438–2449.
[58] Z. Dagan, S. Weinbaum, R. Pfeffer, An infinite-series solution for the creeping motion through an orifice of finite length, J. Fluid Mech. 115 (1982) 505–523.
[59] K. Piroird, C. Clanet, D. Quéré, Capillary extraction, Langmuir 27 (15) (2011) 9396–9402.
[60] P. Marmottant, Effective viscosity of cell aggregates: the role of fluctuations and stress, Proc. Natl. Acad. Sci. USA 12 (2009).
[61] M.A. Swartz, M.E. Fleury, Interstitial flow and its effects in soft tissues, Annu. Rev. Biomed. Eng. 9 (8) (2007) 229–256.
[62] Q.D. Tran, M. Marcos, D. Gonzalez-Rodriguez, Permeability and viscoelastic fracture of a model tumor under interstitial flow, Soft Matter 14 (2018) 6386–6392.
[63] Q.D. Tran, Marcos, D. Gonzalez-Rodriguez, Quantitative characterization of viscoelastic fracture induced by time-dependent intratumoral pressure in a 3D model tumor, Biomicrofluidics 13 (2019) 054107.
[64] D. Ambrosi, S. Pezzuto, D. Riccobelli, T. Stylianopoulos, P. Ciarletta, Solid tumors are poroelastic solids with a chemo-mechanical feedback on growth, J. Elast. 129 (1-2) (2017) 107–124.
[65] L. Kashkooli, D. Rozema, L. Espejo-Ramirez, P. Lasko, F. Fagotto. Ectoderm to mesoderm transition by downregulation of actomyosin contractility. *bioRxiv* (2019).
[66] D. Bonazzi, V. Lo Schiavo, S. Machata, I. Djafer-Cherif, P. Nivoit, V. Manriquez, et al., Intermittent pili-mediated forces fluidize neisseria meningitidis aggregates promoting vascular colonization, Cell 174 (1) (2018) 143–155.
[67] J. Wen, H. Tao, K. Lau, H. Liu, C.A. Simmons, Y. Sun, et al., Cell and tissue scale forces coregulate fgfr2-dependent tetrads and rosettes in the mouse embryo, Biophys. J. 112 (10) (2017) 2209–2218.